Journal of Alloys and Compounds 906 (2022) 164385

Contents lists available at ScienceDirect

Journal of Alloys and Compounds

journal homepage: www.elsevier.com/locate/jalcom

Nanostructure-driven complex magnetic behavior of Sm_2CoMnO_6 double perovskite

Giuseppe Muscas[a,*], K. Prabahar[b], Francesco Congiu[a], Gopal Datt[b], Tapati Sarkar[b,*]

[a] Department of Physics, University of Cagliari, Cittadella Universitaria di Monserrato, S.P. 8 Km 0.700, I-09042 Monserrato, CA, Italy
[b] Department of Materials Science and Engineering, Uppsala University, Box 35, SE-751 03 Uppsala, Sweden

ARTICLE INFO

Article history:
Received 17 December 2021
Received in revised form 13 February 2022
Accepted 25 February 2022
Available online 28 February 2022

Keywords:
Magnetic materials
Strongly correlated systems
Structure-property correlations
Nanostructured functional materials
Magnetic measurements

ABSTRACT

Magnetic double perovskite oxides have steadily emerged as an important class of functional materials. A clear understanding of the complex interactions that govern the magnetic behavior, and thereby, the functionality in these mixed valence compounds, however, remains elusive. In this study, we show that the complex nanostructure that forms in these compounds is at the root of their magnetic behavior. Using complementary experimental and micromagnetic simulation results, we have uncovered the complex nanostructure of polycrystalline Sm_2CoMnO_6, a typical double perovskite oxide, and established how the nanostructure drives its magnetic behavior. Our results show that Sm_2CoMnO_6 exhibits a Griffiths phase with the formation of ferromagnetic clusters above the ordering temperature. The isothermal magnetization curves show no sign of saturation, even at the highest measured field (9 T), and irreversibility in the entire magnetic field range. Despite a very clear indication of the presence of antiferromagnetic antisite defects, surprisingly, no antisite defect-induced exchange bias occurs. This is explained from the micromagnetic simulations that confirm the presence of ferromagnetic nanoclusters and nanosized, random, and uncorrelated antisite defects, resulting in no exchange bias. This work provides a clear understanding of the role of antisite defects, in particular, on how their structure can lead to the presence/absence of exchange bias. The fundamental insight offered in this work fills an important knowledge gap in the field and will be of immense value in realizing the true potential of double perovskite oxides for future technological applications.

1. Introduction

Perovskite oxides, with the general formula, ABO_3, in which A and B are cations, represent an important class of functional materials [1] that have interested the scientific community increasingly over the years due to their unique structural and compositional flexibility, allowing for tunable magnetic and electrical behaviors [2]. Research on these strongly correlated materials is located right at the intersection between fundamental science investigations, striving for a basic understanding of the complex interactions, and technological applications, connected to emergent functionalities. Double perovskites, formed by a "doubling" of the perovskite unit cell, form a sub-family with the general formula $A'A''B_2O_6$ (double A-site) [3] or $A_2B'B''O_6$ (double B-site) [4]. In general, the A-site accommodates an alkali, alkaline earth, or rare-earth metal, while the B-site accommodates 3*d*, 4*d*, or 5*d* transition metals. Magnetic double perovskites have gained their own importance in physics and materials science due to the rich variety of multifunctional properties they exhibit including multiferroicity [5,6], magnetoelectric coupling [7], magnetocapacitance [8], magnetoresistance [8], magnetocaloric effect [9–11], half-metallicity [12], thermoelectric properties [13–15], and exchange bias [16–18]. Furthermore, they are a perfect platform to study the physics behind the complex interactions that give rise to such exotic properties. In the rare-earth based transition metal double perovskites of the form $R_2M'M''O_6$, where R is the rare-earth cation and M′ and M″ are transition metal cations, these different magnetic phenomena have their origin in oxygen-mediated cationic exchange interactions. In addition, the transition metal ions often present mixed valence states. Antiphase boundaries and antisite defects between the mixed valence magnetic ions are also believed to play a major role in determining the magnetic behavior [19,20]. Thus, apart from the choice of the M′ and M″ ions, the magnetic behavior is affected by the local ordering of these ions. While the existence of antisite defects has been confirmed via first

* Corresponding authors.
E-mail addresses: giuseppe.muscas@dsf.unica.it (G. Muscas), tapati.sarkar@angstrom.uu.se (T. Sarkar).

https://doi.org/10.1016/j.jallcom.2022.164385
0925-8388/

principle calculations [21,22], their exact role in determining the magnetic behavior in these complex quaternary oxides is yet to be understood.

The R_2CoMnO_6 (R = La,…, Lu) compounds form a subclass of the magnetic double perovskites, where, in the ideal ordered structure, the alternating Co^{2+} and Mn^{4+} ions lead to long-range ferromagnetic (FM) ordering. The ferromagnetic Curie temperature decreases with the size of the rare-earth ion from T_C = 48 K for Lu_2CoMnO_6 to T_C = 204 K for La_2CoMnO_6 [23]. On the other hand, incomplete alternation of Co^{2+} and Mn^{4+} ions results in local antisite defects where Co^{2+}-O-Co^{2+} or Mn^{4+}-O-Mn^{4+} arrangements lead to antiferromagnetic (AFM) interactions [24,25]. Antiferromagnetic ordering involving the valence states Co^{3+}O-Mn^{3+} can also occur [26]. The balance between the different ionic valence can depend on synthesis conditions and particle size [27]. Furthermore, doping at the Co and/or Mn sites also affects the magnetic properties [28,29].

In this work, we report a combined experimental and micromagnetic simulation exploration with the aim of understanding the origin of the complex magnetic behavior of polycrystalline Sm_2CoMnO_6. Sm_2CoMnO_6 occurs approximately midway between the series R = La,…., Lu and accordingly has a T_C ~135 K [23,30]. It is a type-II multiferroic material, while also exhibiting other exotic magnetic properties like metamagnetism [30,31] and huge spontaneous exchange bias (on doping at the Sm-site) [32]. The sample in this work was prepared using a conventional solid-state reaction method. Despite the expected presence of antisite defects, our sample shows a marked absence of exchange bias, contrary to usual expectations of antisite defects being a source for exchange bias [33,34]. This unusual behavior is later explained from our micromagnetic simulation results. This work provides a platform for a deeper understanding of the role of the ubiquitous antisite defects in double perovskite systems, in particular, on the presence/absence of exchange bias in these systems. In the following sections, we first present the synthesis and structural and morphological characterization of polycrystalline Sm_2CoMnO_6, followed by detailed magnetic measurements and micromagnetic simulations.

2. Methods

2.1. Sample preparation

Polycrystalline Sm_2CoMnO_6 was prepared via a conventional solid-state reaction method. Stoichiometric amounts of Sm_2O_3, $CaCo_3$, Co_3O_4, and Mn_2O_3 with a purity of 99.9% (from Sigma Aldrich) were mixed using a ball mill and calcined at 1200 °C. The obtained powder was ground and pressed into cylindrical green compacts and subjected to sintering at 1350 °C for 12 h in air. After sintering, the pellets were slowly cooled to 500 °C at a rate of 1 °C /min, and then furnace cooled to room temperature. More details of the synthesis steps are provided in the electronic supplementary information (Supplementary Material).

2.2. X-ray diffraction measurement and data analysis

The sample was structurally characterized using X–ray powder diffraction (XRPD), acquired at room temperature using a Siemens D5000 diffractometer with Cu-Kα radiation (λ = 1.5418 Å). The diffraction pattern was recorded over the range of 2θ = 10–90° with a step size of 0.02°. Structural refinements were performed by the Rietveld method using the MAUD software [35]. The refinement was done on the Crystalline Open Database entry 4514503 reported for monoclinic La_2CoMnO_6 with space group $P2_1/n$ [36], and for the entry 7029461 for orthorhombic Y_2FeMnO_6 *Pnma* [37], after adjusting the two structures to the Sm_2CoMnO_6 composition. The refinement was corrected for the instrumental broadening, estimated from the refinement of a standard Al_2O_3 sample.

2.3. Scanning electron microscopy and X-ray photoelectron spectroscopy

The surface morphology of the sintered pellet was analyzed using a field emission scanning electron microscope (FESEM, Carl Zeiss, LEO1550 model) at an operating voltage of 3–5 kV and magnification of 5–8 kX. The images were collected in secondary electron mode. The compositional analysis of the sample was performed via energy dispersive X-ray (EDX) analysis attached to the FESEM. Room temperature X-ray photoelectron spectroscopy (XPS) measurements were performed using a physical electronics Quantera II XPS with monochromatic Al operated at 15 kV with a total power of 50 W. The spot size was 100 µm. The base pressure in the measurement chamber was maintained at approximately 7×10^{-7} Torr. The high-resolution XPS was obtained with 55 eV pass energy. All the spectra were calibrated using the carbon peak.

2.4. Magnetic measurements and simulations

Magnetic measurements were performed using a physical property measurement system-based vibrating sample magnetometer from Quantum Design Inc. Magnetization versus temperature scans (in zero field cooled (ZFC) and field cooled (FC) modes) were recorded in the temperature range 5–380 K, while isothermal magnetization curves were recorded in the magnetic field range + 9 T to - 9 T. To eliminate the small residual field in the instrument, before each measurement, we applied a manual degauss process with an oscillating field. At the end of the degauss process, the effective residual field was estimated to be smaller than +/- 0.1 Oe. The micromagnetic model of the sample was developed with the GPU accelerated micromagnetic software MuMax3 [38], which solves the Landau-Lifshitz-Gilbert (LLG) equation using a finite-difference discretization method.

3. Results and discussion

3.1. Structural and morphological characterization

Scanning electron microscopy (SEM) analysis reveals the presence of agglomerates of multiple grains (2–5 µm in size, Fig. 1a). The individual grains are visible at higher magnification (Fig. 1b). Their size distribution can be described by a lognormal curve (Fig. 1c) that shows an average size of approximately 1140(20) nm, with a large standard deviation of 410(20) nm.

The X-ray powder diffraction (XRPD) pattern of the sample (Fig. 1d) reveals the presence of a single phase, with a monoclinic structure (space group $P2_1/n$), as observed for bulk single crystals [23]. The results of the Rietveld refinement confirm the polycrystalline nature of each grain, constituted of crystalline domains of size approximately 190 nm. The results of the refinement are reported in Table 1. Alternative refinements using an orthorhombic structure (space group *Pnma*), or a mixture of monoclinic and orthorhombic structures did not provide better results (see Supplementary Material for detailed information).

Room temperature energy dispersive X-ray (EDX) analysis confirmed that the stoichiometry of the sample (metal cations) was in accordance with the nominal composition. Oxygen was not considered because the EDX technique is not suitable for quantifying light elements.

X-ray photoelectron spectroscopy (XPS) measurements reveal that the Co and Mn peaks are deconvoluted into multiple components evidencing multiple valence states [39]. The experimental and fitted Mn-2p, Co-2p, and Sm-3d core-level spectra of Sm_2CoMnO_6 are shown in Fig. 2a-c. The measured XPS spectra were analyzed and fitted with a combination of Gaussian and Lorentzian functions; this combination minimizes the least-square fitting error. Further, a

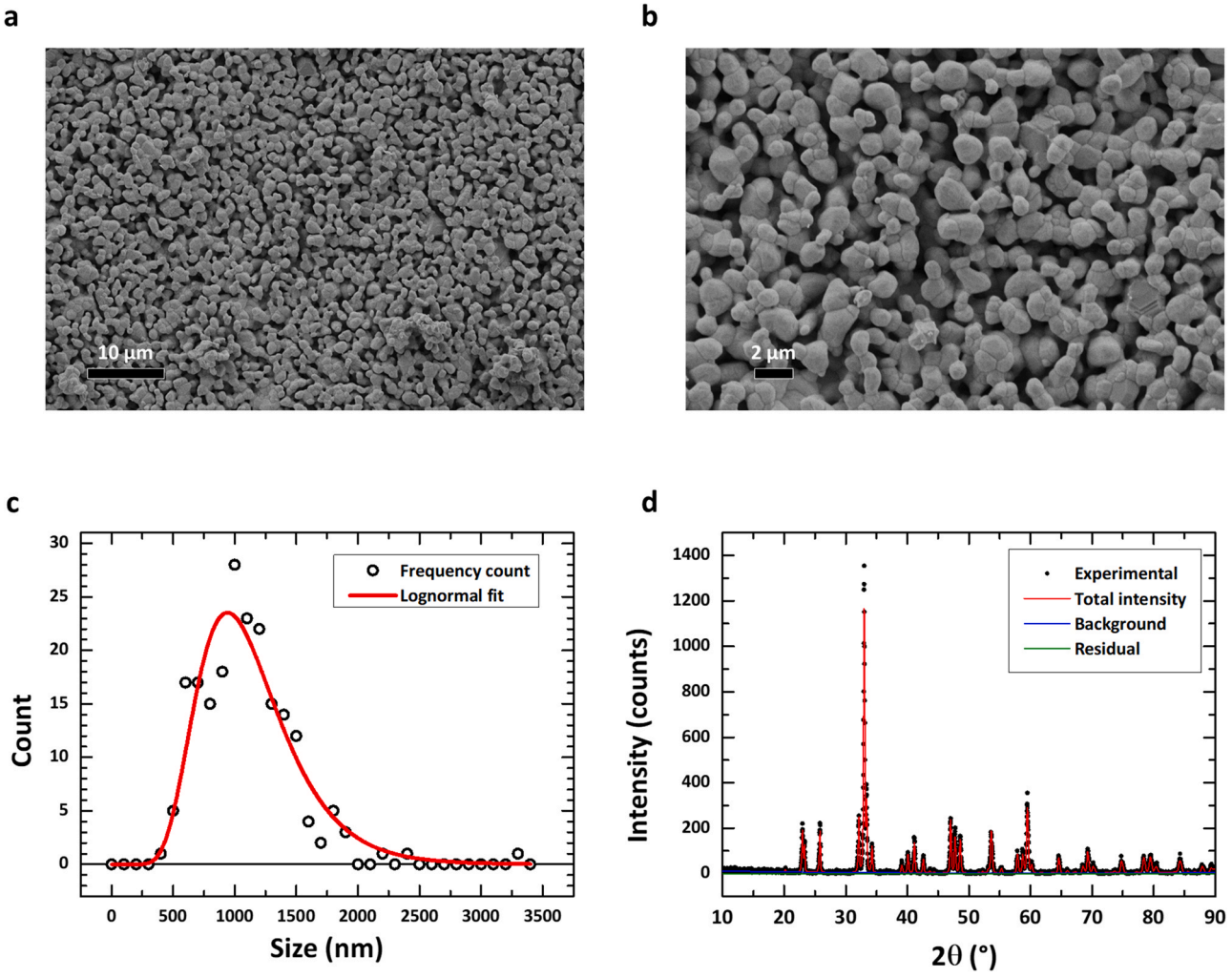

Fig. 1. Structural and morphological characterization of polycrystalline Sm_2CoMnO_6: SEM micrographs using a (a) lower and (b) higher magnification, (c) size distribution estimated from the SEM micrographs, and (d) XRPD pattern along with the Rietveld refinement fit and residues.

Table 1
Results of Rietveld refinement of XRPD pattern of polycrystalline Sm_2CoMnO_6.

Parameter	Value
a	5.3612(2) Å
b	5.5636(2) Å
c	7.6105(3) Å
Angle β	90.01(4)°
Crystallite size	188(6) nm
Microstrain	0.00099(2)
Density	7470 kg m^{-3}
R_{wp}	24.05%
R_{exp}	20.27%

linear-type background function was used for the elimination of the inelastic background from the obtained XPS spectra. XPS spectrum of Mn-2p is shown in Fig. 2a. The Mn-2p spectrum consists of two distinct asymmetrical peaks located at 641 and 653 eV which correspond to the Mn-2$p_{3/2}$ and 2$p_{1/2}$ resulting from the spin-orbital splitting of the 2p orbitals [40,41]. Further, the Mn-2$p_{3/2}$ peak is deconvoluted into three components at the binding energies of 640.7, 641.8, and 643.7 eV corresponding to Mn^{2+}, Mn^{3+}, and Mn^{4+}, respectively. These results match with reported literature [42–44]. Similarly, the spin-orbital splitting of Co-2p consists of two main peaks located at 780 and 795 eV, corresponding to Co-2$p_{3/2}$ and Co-2$p_{1/2}$ along with two satellite peaks beside the Co-2p [45,46], as shown in Fig. 2b. The deconvolution of Co-2$p_{3/2}$ results in two components at the binding energies of 779.7 and 781.7 eV, ascribable to the Co^{3+} and Co^{2+} states, respectively [47]. On the other hand, spin-orbit splitting of Sm-3$d_{5/2}$ and 3$d_{3/2}$ are found at 1082 and 1109 eV confirming that Sm exists in +3 oxidation state [48]. The XPS results thus confirm that in our sample, both Mn and Co exist in mixed valence states. In the case of cobalt, Co^{2+} and Co^{3+} signals have an area ratio of 0.357:0.643. For manganese, the spectrum evidences the presence of Mn^{2+}, Mn^{3+}, and Mn^{4+} with a relative proportion of 0.1852, 0.5848, and 0.2300. Further details of the XPS analysis are provided in the Supplementary Material.

3.2. Magnetization measurements

Fig. 3a shows zero-field cooled (ZFC) and field-cooled (FC) curves recorded under a magnetizing field of 2.5 mT. They reveal a ferromagnetic-like signal (increase in magnetization) below approximately 153 K (also seen in Fig. 3b, where we show the evolution of dM/dT versus T), with irreversibility between the two curves setting in from below 147 K. On cooling, the ZFC curve shows a peak at 135 K followed by a reduction in magnetization that finally reaches a plateau at lower temperatures. The ordering temperature T_C, defined as the temperature at which the ZFC dM/dT versus T curve has the largest negative peak, is estimated at ~140 K (Fig. 3b).

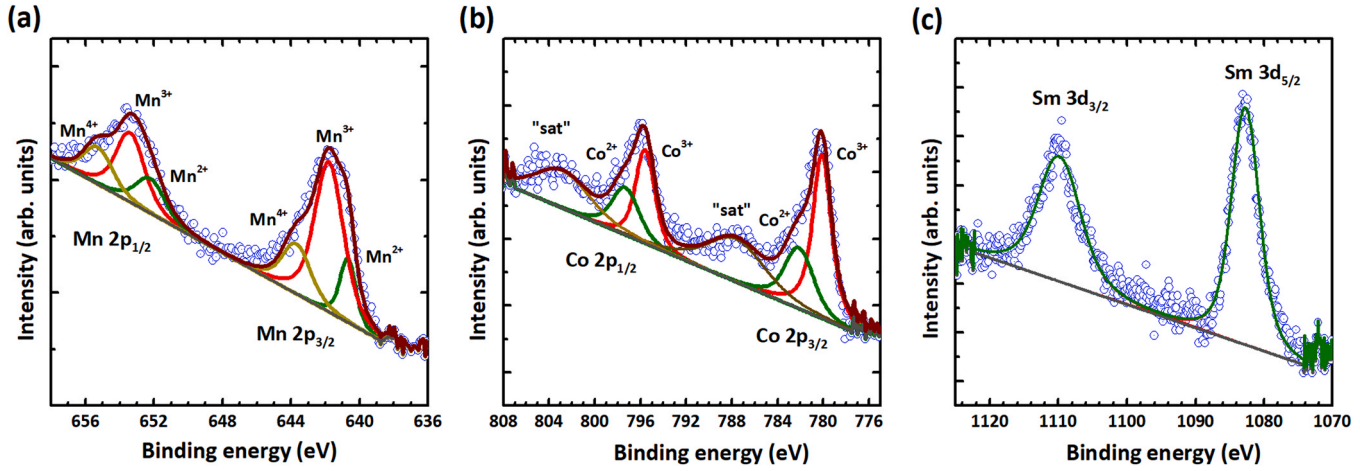

Fig. 2. XPS core level spectra of Sm_2CoMnO_6 of (a) Mn-2p core level spectra, (b) Co-2p core level spectra, and (c) Sm-3d core level spectra. The blue circles indicate the experimental data and the solid lines are the respective fitted peaks.

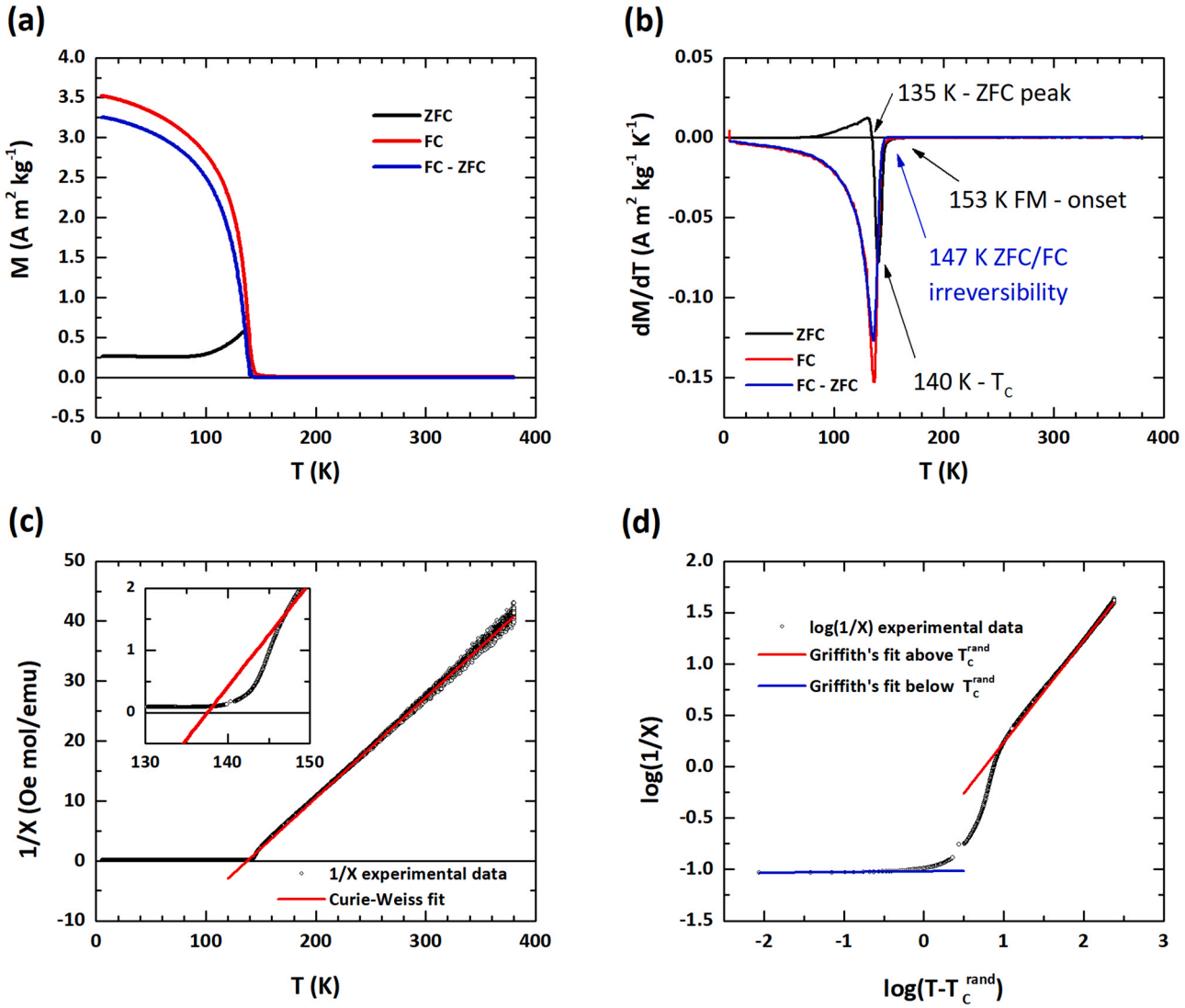

Fig. 3. Effect of temperature on the magnetic behavior of polycrystalline Sm_2CoMnO_6: (a) ZFC and FC M versus T curves recorded under a low magnetizing field of 2.5 mT, (b) the corresponding dM/dT versus T curves, (c) inverse susceptibility plot along with the Curie-Weiss fit. The inset shows the expanded region around the ordering temperature, (d) log-log plot of χ^{-1} versus $(T-Tc^{rand})$, see text for details.

The inverse susceptibility data in the high-temperature region (T > 200 K) was used for performing a fit using the Curie-Weiss law, $\chi = C/(T-\theta_{CW})$. The fit (Fig. 3c) yields a positive Curie-Weiss temperature, θ_{CW} = 136.6(4) K, which is very close to the ordering temperature. From the Curie constant, C, we obtained an effective paramagnetic moment of 6.900(2) μ_B/f.u. The theoretical moment per formula unit for Sm_2CoMnO_6 can be calculated from the formula [49]:

$$\mu_{eff} = \sqrt{\sum p_x {\mu_x}^2} \quad (1)$$

where p_x and μ_x are the populations and ion moments of each cation. Considering 3.87 μ_B and 4.90 μ_B for the high spin states of Co^{2+}/Co^{3+}, 5.92 μ_B, 4.90 μ_B, and 3.87 μ_B for $Mn^{2+}/Mn^{3+}/Mn^{4+}$, respectively, and 0.85 μ_B for Sm^{3+} [50], the result corresponds to a theoretical moment of 6.80 μ_B/f.u, which is compatible with the value extrapolated from the experimental results of Kim et al. on single crystalline Sm_2CoMnO_6 [23], but lower than the experimental value from the Curie-Weiss fit. The result can be explained considering the presence of a Griffiths phase, i.e., the formation of ferromagnetic clusters above the long-range ordering temperature. Thus, the presence of short-range ferromagnetic clusters in the paramagnetic state is responsible for the enhanced effective paramagnetic moment [51].

The Griffiths phase can be characterized by the downturn deviation from the Curie-Weiss law behavior of the χ^{-1} curve on cooling from above the long-range ordering temperature [52]. This downturn deviation is evident in the inset of Fig. 3c and it is analyzed in Fig. 3d. One can fit the χ^{-1} curve with the equation:

$$\frac{1}{\chi} = \frac{(T - T_C^{rand})^{1-\lambda}}{G} \quad (2)$$

where G and λ are free parameters, and T_C^{rand} represents the critical temperature of the random ferromagnetic cluster formation, where the susceptibility tends to diverge. Although a full consensus in interpreting the physical meaning of T_C^{rand} is still to be reached within the scientific community, by definition, T_C^{rand} should lie between the actual ordering temperature T_C and the highest ordering temperature of any ferromagnetic cluster. Hence, fitting the χ^{-1} curve slightly above and below such temperature should identify the two extreme conditions: a pure paramagnetic system with $\lambda \approx 0$, and a randomly clustered ferromagnetic one with $\lambda \approx 1$. This assumes a correct estimation of T_C^{rand} [52]. In oxides, T_C^{rand} is found to be very close to the Curie-Weiss temperature θ_{CW} [39], hence one can use $T_C^{rand} = \theta_{CW}$. Thus, using T_C^{rand} = 136.6 K, we have plotted χ^{-1} as a function of $(T-T_C^{rand})$ in a log-log scale (Fig. 3d). The fit of χ^{-1} in the two regimes yielded λ = 0.0093(5) and 0.994(1), above and below T_C^{rand}, respectively. These results strongly support the presence of a Griffiths phase in the sample.

The M-H curve recorded at T = 5 K is shown in Fig. 4a. The system shows no sign of saturation, even at the highest measured field of 9 T. Considering the calculated theoretical effective moment of 6.80 μ_B/f.u. and the density of 7470 kg m^{-3} obtained from the Rietveld refinement, the saturation magnetization for an ordered ferromagnetic arrangement should be 74 Am^2 kg^{-1}. This value is much higher than what is achieved in our sample at 9 T. In addition, the M-H curve exhibits irreversibility up to a very high field.

The reduced value of magnetization as compared to the theoretical maximum moment is explained by the fact that, apart from the ideal ordered structure with only ferromagnetic Co-O-Mn interchains, the structure also has Co-O-Co, Mn-O-Mn, and Co-O-Mn antiferromagnetic chains [33] arising from the exchange of the Co/Mn positions forming the so-called antisite defects [39]. The presence of antiferromagnetic order not only decreases the net magnetization but also creates competition with the ferromagnetic order, thereby reducing the ordering temperature and promoting frustration and metamagnetism [30]. The observed M-H curve is a result of this complex framework of magnetic ordering.

The M-H curve evolves as a function of temperature (selected temperatures shown in Fig. 4b), showing a typical reduction in the remanent magnetization (M_R) and coercivity (H_C) (Fig. 4c), with the disappearance of the hysteretic behavior near the ordering temperature (~140 K). However, the M-H curves recorded above the transition temperature still retain an "S" shape, and a perfect paramagnetic behavior is observed only for temperatures ≥ 200 K. This observation agrees with the presence of local random ferromagnetic clusters in a Griffiths phase slightly above the long-range ordering temperature (T_C).

The presence of antisite defects has usually been understood as a source of exchange bias in double perovskites [34,53]. As such, we carefully checked for the presence of exchange bias in our sample by measuring M-H loops at 5 K after field cooling (FC) the sample under applied fields of + 3 T and − 3 T. Interestingly, despite the most likely presence of antisite defects responsible for the strongly reduced magnetization, we observed no exchange bias in the sample (Fig. 4d), with the FC processes leaving no trace in the subsequent M-H curves.

3.3. Micromagnetic modelling

To explain our unexpected observation of lack of exchange bias in the sample, and to gain a deeper understanding of the mechanism of magnetization reversal in these complex systems, we performed micromagnetic simulations. We based our model on the assumption that all the magnetic properties are determined by the internal structure of each crystalline grain. To reproduce the micromagnetic structure, we used supra-grains representing the large crystalline coherent domains. The experimental evidence of the Griffiths phase indicates the presence of regions, typically few tens of nm in size [54], with variable local ferromagnetic exchange with respect to the average long-range ferromagnetic ordering. To include this clustered internal structure, each supra-grain is divided by Voronoi tessellation [55] into internal magnetic sub-grains. Inside each cluster, a general FM order is established with a positive value of exchange stiffness which varies according to a Gaussian distribution, to account for the Griffiths phase behavior. Such clusters have uniaxial magnetocrystalline anisotropy with anisotropy constant (K_u) varying in each cluster according to a log-normal distribution with a defined average and standard deviation (STD). All clusters in each supra-grain share the same easy axis. This allows us to preserve the crystalline continuity of the supra-grain while introducing the variability due to local chemical inhomogeneity arising from the mixed valence states. The supra-grain size was investigated in the range 192–48 nm with no significant variation in the results besides the statistical random noise. For optimization of the code, we used 128 nm cubic supra-grains (Fig. 5a) with evident speed-up of the calculations, but without compromising the accuracy or quality of the results (Fig. S2a in the Supplementary Material). Similarly, we analyzed the cluster size effect in the range 50–5 nm, observing similar behavior in the range 50–20 nm, and a sharp magnetization reversal, not compatible with the round and smooth curve observed experimentally, only for 10 and 5 nm clusters (Fig. S2b in the Supplementary Material). According to these results, we used an intermediate size of 30 nm, in agreement with the observation of Asaka et al. [54]. Each simulation run used a block of 8 supra-grains, repeated with periodic boundary conditions 10 times in both positive and negative X-Y-Z spatial directions. This improves the statistics and allows us to consider long-range interactions. Finally, the model was simulated 5 times with different initial seed, to produce 5 different random configurations. It is worth noting that to reproduce the system correctly, it was discretized in cubic cells with an edge of 2.00 nm, smaller than the exchange length, 2.27 nm, determined by the weakest exchange

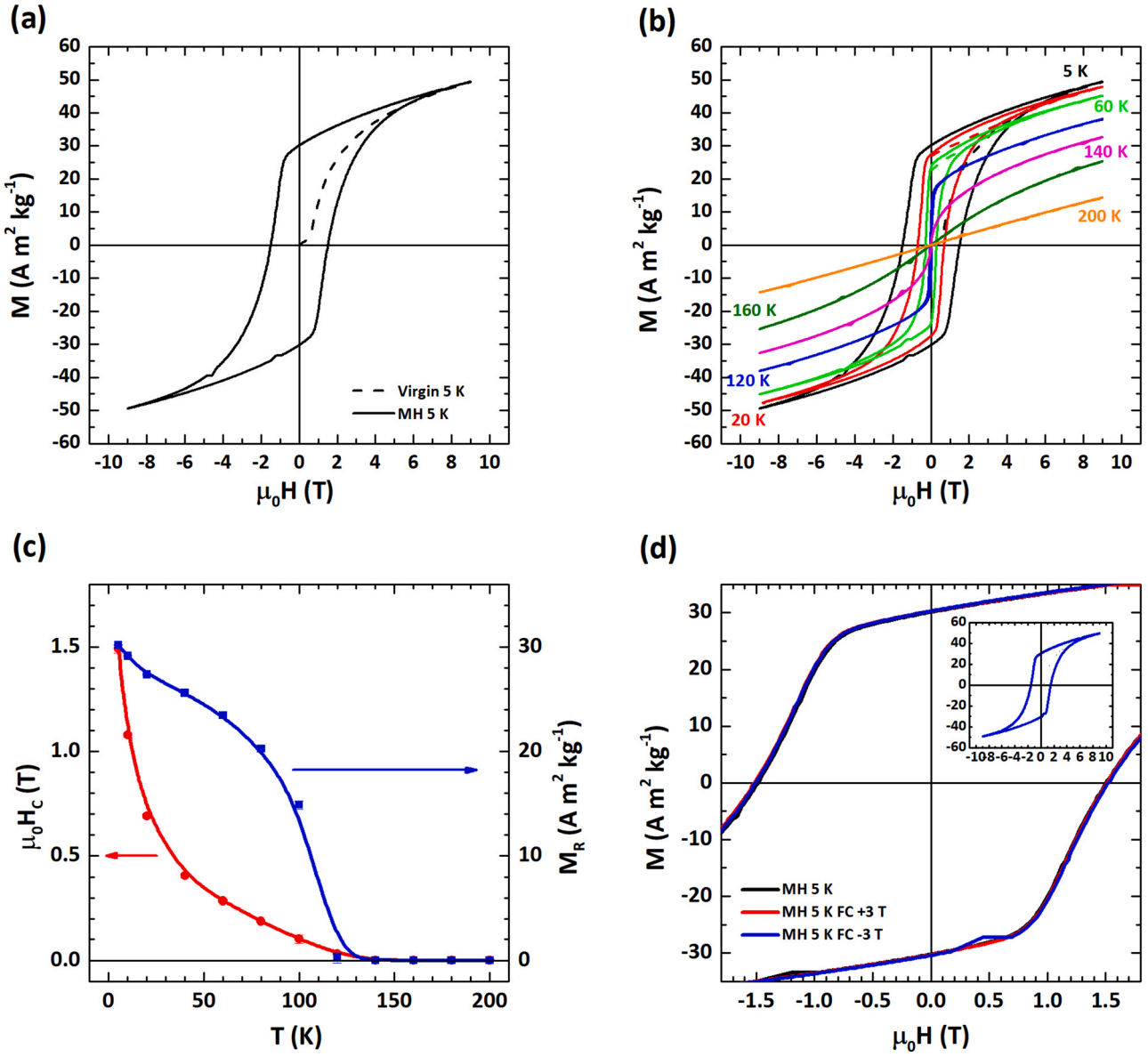

Fig. 4. Effect of magnetic field on the magnetic behavior of polycrystalline Sm_2CoMnO_6: isothermal magnetization curve recorded at (a) T= 5 K and (b) different selected temperatures after zero field cooling, (c) evolution of the remanent magnetization and coercivity with temperature, and (d) isothermal magnetization curve recorded at T = 5 K after zero field cooling and field cooling with applied fields of ± 3 T.

stiffness value among the ferromagnetic clusters, and smaller than the domain wall width determined by the large magneto-crystalline anisotropy (2.76 nm) [56].

To explain the observed lack of saturation magnetization even at 9 T we need to include the presence of antiferromagnetic elements. Within the framework of micromagnetic simulations, although one cannot include AFM interactions at the atomic scale, we have created effective AFM inclusions using individual cells with AFM exchange interactions with the neighboring ones. The antiferromagnetic defects (AFM cells) have random direction of the anisotropy axis to create a frustrated structure, as is usually observed in this kind of double perovskites [33,57–59]. To reproduce the sample, all cells have a value of magnetization corresponding to the theoretical value of 74 Am^2kg^{-1} for full parallel FM ordering. In this way, the amount of AFM cells has been optimized in order to produce a final effective magnetization such as recorded in the experimental M(H) curve.

The micromagnetic model was optimized by adjusting the AFM cells amount, the exchange, and the anisotropy parameters, so as to reproduce the experimental *M-H* loop at 5 K. The optimized exchange stiffness (A_{ex}) inside each magnetic cluster is approximately 3.0 pJ/m (STD 0.5 pJ/m), reasonably smaller than 4–5 pJ/m, reported for $La_{0.7}Sr_{0.3}MnO_3$, which has a larger T_C [60,61]. At the cluster boundaries, A_{ex} is calculated by the software as the harmonic mean of the individual values of the adjacent clusters. This distribution of A_{ex} values among clusters allows ferromagnetic ordering of some of them above the long-range bulk ferromagnetic ordering of the structure, as in the Griffiths phase model. Finally, the optimal amount of antiferromagnetic cells is found to be 20% of the total amount. The AFM cells are coupled to the ferromagnetic clusters with an exchange stiffness of - 3.0 pJ/m (STD 0.5 pJ/m). The best results were obtained for 30 nm FM clusters with a lognormal distribution of anisotropy constant with a mean value of 1.8 MJ/m^3 and a standard deviation of 0.8 MJ/m^3 (all relevant parameters are summarized in Table 2).

The simulation of the *M-H* loop was repeated also after a simulated field cooling process. The effect of thermal fluctuations is introduced in MuMax3 via a stochastic thermal field [62]. While thermal fluctuations act on each individual atomic spin, in the

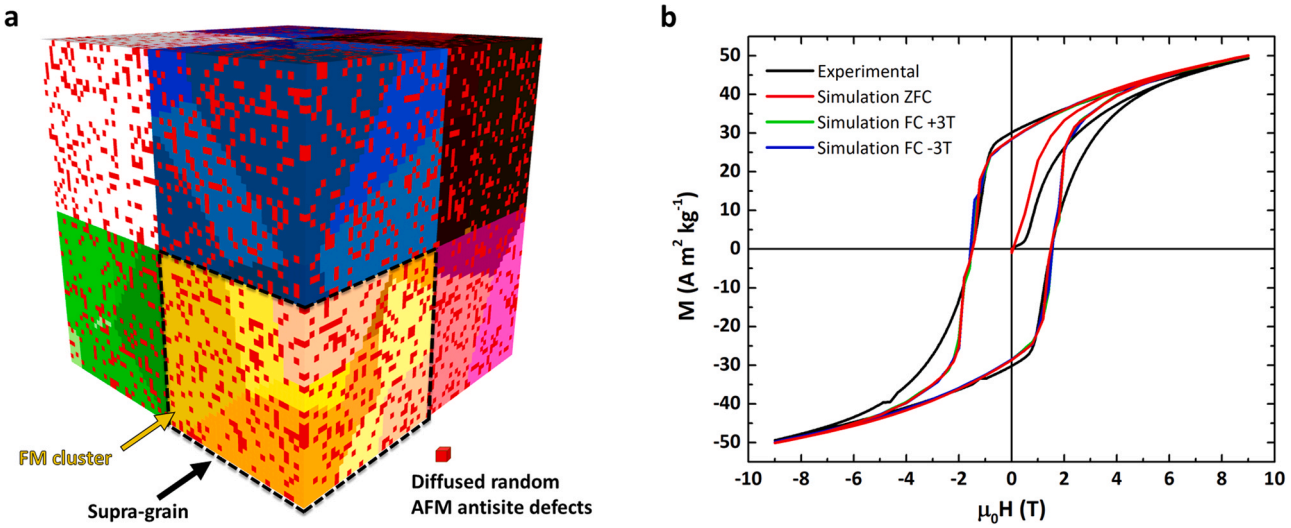

Fig. 5. (a) Model used for micromagnetic simulation (for details, see text) and (b) comparison between the experimental and simulated M-H curves.

micromagnetic simulation, the stochastic field acts on single cells. This typically causes an overestimation of the critical ordering temperatures. Nonetheless, the simulated temperature T_{sim} can be compared to the experimental value T_{exp} by taking into account the ratio between the simulation cell size a_{cell} and the interatomic distances, such as, for cubic crystals, the lattice parameter a_{lat} [63]:

$$T_{sim} \approx \frac{a_{cell}}{a_{lat}} T_{exp} \quad (3)$$

and it can be scaled to compare the results qualitatively. We have applied a simulated temperature large enough to overcome any exchange interaction. Then, with an applied field of + 3 T or − 3 T, the temperature was reduced to zero reproducing a conventional field cooling process.

The presence of antiferromagnetic order in micromagnetic simulations can be a controversial aspect. Indeed, the micromagnetic theory assumes that the exchange among two adjacent spins is valid only if their angle is < 25°. However, in the present model, the antiferromagnetic elements represent defects and can be approximated as effective canted antiferromagnetic elements where the continuity of the magnetization is not valid. Moreover, MuMax3 calculates the exchange energy density from the cosine of the angle, such as in the Heisenberg atomistic model, thus allowing a correct estimation of the exchange energy even in the non-continuous model [64].

As can be observed in Fig. 5b, our simulations yield a good correlation with the experimentally observed *M-H* curves, describing accurately both the coercivity and remanent magnetization, as well as the magnetization reversal at high field, with visible irreversibility up to the maximum applied field (see Fig. S3 in Supplementary Material). Furthermore, the *M-H* loops simulated after the field cooling protocol using both + 3 T and − 3 T resulted in no exchange bias or any other effect, in agreement with our experimental observations. These results confirm the accuracy of our model, which in turn proves that the magnetization reversal in polycrystalline Sm_2CoMnO_6 is the product of a complex nanostructure. The main contribution comes from FM nanoclusters with large magnetocrystalline anisotropy, with the additional partial realignment of canted antiferromagnetic local defects. An example of magnetization reversal for a typical random seed is described in the video provided in the Supplementary Material. Most importantly, such antiferromagnetic antisites represent random and uncorrelated point-defects and, for this reason, they do not lead to any exchange bias.

To verify our model and conclusions unambiguously, we have performed additional simulations with alternative models, refining the structure, anisotropy, and exchange values to obtain the best possible reproduction of the experimental M(H) curve. The simplest alternative is to use ferromagnetic clusters with very high anisotropy. The hypothesis here is that the measured *M-H* curve is a simple minor loop. To obtain a reduced magnetization and reproduce the high field reversal of the experimental *M-H* curve, one needs to set the average anisotropy constant to 6.5 MJ/m^3 with a very large STD of 5.0 MJ/m^3. However, this model yields a too large coercivity value, a spontaneous exchange bias shift of the *M-H* curve, and a strong conventional exchange bias effect using FC with + 3 T and − 3 T protocols (Fig. S4a in the Supplementary Material).

A second alternative model could be used considering that the high field irreversibility and low experimental magnetization are the results of local canted ferromagnetic elements with extremely high magnetic anisotropy. This model can reproduce only in part the experimental zero field cooled *M-H* curve, when optimized using the same anisotropy for the main FM cluster K_u = 1.8 MJ/m^3 (STD = 0.8 MJ/m^3) and introducing 50% of the volume in a randomly canted configuration with average K_u^{canted} = 14.0 MJ/m^3 (STD = 5.0 MJ/m^3). However, even in this case, there is a clear spontaneous exchange bias, and the FC protocol leads to an even larger conventional exchange bias with both a horizontal and vertical shift (Fig. S4b in the Supplementary Material).

Table 2
Magnetic parameters used for the micromagnetic simulation; FM = ferromagnetic, AFM = antiferromagnetic, STD = standard deviation.

Simulation parameters	Value
M_S	555 kA/m
K_u	Mean 1.8 MJ/m^3, STD 0.8 MJ/m^3
A_{ex} FM clusters	Mean 3.0 pJ/m, STD 0.5 pJ/m
A_{ex} AFM cells	Mean − 3.0 pJ/m, STD 0.5 pJ/m
A_{ex} among AFM cells and between FM clusters and AFM cells	Mean − 3.0 pJ/m, STD 0.5 pJ/m

We have also reproduced the sample using a third alternative model, without random uncorrelated antiferromagnetic elements, using instead an effective antiferromagnetic ordering in part of the magnetic clusters. This model can reproduce the ZFC M-H curve reducing cluster size to 20 nm, fixing AFM order in 45% of them, and using a common value of K_u = 2.0 MJ/m^3 (STD = 0.8 MJ/m^3) for the ferromagnetic and antiferromagnetic ones. However, the model is sensitive to the FC protocols, showing a reduction of remanent magnetization value in the corresponding M-H curves (Fig. S4c in the Supplementary Material). Indeed, the FC process improves the order at the antiferromagnetic interfaces created among the ferromagnetic and antiferromagnetic clusters resulting in a clear extra demagnetization effect. This behavior is in stark contrast to the experimental results (Fig. 4**d**), and hence, this cannot be the correct model for our sample.

Thus, our initial model using a minor antiferromagnetic phase consisting of random uncorrelated antiferromagnetic elements (antisite defects) is the correct one and provides a clear explanation of the simultaneous reduction in magnetization from the theoretically expected value and the unexpected absence of exchange bias. As observed by Coutrim and coworkers [65], undoped double perovskites show the coexistence of FM and AFM superexchange interactions, nevertheless, with a lower degree of frustration with respect to the relative doped versions, where the uncompensated AFM couplings between Co and Mn lead to spin-glass like behavior resulting in spontaneous exchange bias [66]. Similar conclusions have been proposed in several experimental investigations on doped double perovskites [32,34,58]. These results are in line with our model, which assumes the presence of AFM antisite defects, as suggested by the experimental magnetization curves, but their point-like diffuse and uncorrelated presence, as confirmed by micromagnetic simulations, is not sufficient for the occurrence of the exchange bias phenomenon. Additional investigation will be needed to clarify the role of doping on the magnetic nanostructure and how this connects to exchange bias. Finally, our model also reproduces the observed temperature dependence of magnetization reasonably well, within the limits of the micromagnetic simulation approach (Fig. S5 in the Supplementary Material), thereby providing additional confirmation of the validity of the model.

4. Conclusions

In summary, via a combined experimental/micromagnetic simulation approach, we have provided a detailed understanding of the complex magnetic behavior of Sm_2CoMnO_6 that arises as a direct result of its complex nanostructure. The sample exhibits a Griffiths phase with the presence of ferromagnetic nanoclusters above the ordering temperature. Despite the presence of antiferromagnetic antisite defects in the system (leading to a non-saturating *M-H* curve even at very high fields), there is no antisite defect-induced exchange bias. This apparent inconsistency is explained by the micromagnetic simulations that reveal that such antiferromagnetic antisites can be modeled as random and uncorrelated point-defects, which do not lead to exchange bias. Alternative models using ferromagnetic clusters with very high anisotropy, local canting of the ferromagnetic moments, and extended antiferromagnetic clusters do not reproduce the experimentally observed *M-H* curves, confirming that our model based on random, uncorrelated antiferromagnetic elements (antisite defects) is the correct one. This work provides a clear understanding of the role of antisite defects in double perovskite systems, and, in particular, their effect on the presence/absence of exchange bias. The fundamental insight gained in this work will be of great value in the future use of double perovskite oxides in emergent technological applications.

CRediT authorship contribution statement

Giuseppe Muscas: Conceptualization, Investigation, Validation, Formal analysis, Writing – original draft, Writing – review & editing. **K. Prabahar:** Investigation, Validation, Formal analysis, Writing – original draft, Writing – review & editing. **Francesco Congiu:** Investigation, Validation, Formal analysis, Writing – original draft, Writing – review & editing. **Gopal Datt:** Investigation, Validation, Formal analysis, Writing – original draft, Writing – review & editing. **Tapati Sarkar:** Conceptualization, Writing – original draft, Writing – review & editing, Supervision, Project administration, Funding acquisition.

Declaration of Competing Interest

The authors declare that they have no known competing financial interests or personal relationships that could have appeared to influence the work reported in this paper.

Acknowledgements

We gratefully acknowledge funding from Stiftelsen Olle Engkvist Byggmästare (grant number: 200-0559), Carl Tryggers Stiftelse för Vetenskaplig Forskning (grant number: CTS 18:340), the Royal Physiographic Society of Lund (the Märta and Eric Holmberg Endowment), and the Swedish Research Council (grant numbers: 2017-05030 and 2021-03675). G. M. acknowledges financial support from the PON AIM program (Project AIM1809115 – Activity No. 3 - Line 2.1). G. M. and F. C. acknowledge the CeSAR (Centro Servizi d'Ateneo per la Ricerca) of the University of Cagliari (Italy) for SEM, EDX, and magnetometry experiments.

Appendix A. Supporting information

Supplementary data associated with this article can be found in the online version at doi:10.1016/j.jallcom.2022.164385.

References

[1] C. Sun, J.A. Alonso, J. Bian, Recent advances in perovskite-type oxides for energy conversion and storage applications, Adv. Energy Mater. 11 (2021) 2000459, https://doi.org/10.1002/aenm.202000459
[2] Y. Gao, J. Wang, L. Wu, S. Bao, Y. Shen, Y. Lin, C. Nan, Tunable magnetic and electrical behaviors in perovskite oxides by oxygen octahedral tilting, Sci. China Mater. 58 (2015) 302–312, https://doi.org/10.1007/s40843-015-0047-0
[3] J. Young, J.M. Rondinelli, Improper ferroelectricity and piezoelectric responses in rhombohedral (A,A′)B_2O_6 perovskite oxides, Phys. Rev. B. 89 (2014) 174110, https://doi.org/10.1103/PhysRevB.89.174110
[4] S. Vasala, M. Karppinen, $A_2B'B''O_6$ perovskites: a review, Prog. Solid State Chem. 43 (2015) 1–36, https://doi.org/10.1016/j.progsolidstchem.2014.08.001
[5] S. Chikara, J. Singleton, J. Bowlan, D.A. Yarotski, N. Lee, H.Y. Choi, Y.J. Choi, V.S. Zapf, Electric polarization observed in single crystals of multiferroic Lu2MnCoO6, 180405(R), Phys. Rev. B. 93 (2016), https://doi.org/10.1103/PhysRevB.93.180405
[6] N. Terada, D.D. Khalyavin, P. Manuel, W. Yi, H.S. Suzuki, N. Tsujii, Y. Imanaka, A.A. Belik, Ferroelectricity induced by ferriaxial crystal rotation and spin helicity in a B-site-ordered double-perovskite multiferroic In_2NiMnO_6, Phys. Rev. B. 91 (2015) 104413, https://doi.org/10.1103/PhysRevB.91.104413
[7] N. Lee, H.Y. Choi, Y.J. Jo, M.S. Seo, S.Y. Park, Y.J. Choi, Strong ferromagnetic-dielectric coupling in multiferroic Lu_2CoMnO_6 single crystals, Appl. Phys. Lett. 104 (2014) 112907, https://doi.org/10.1063/1.4869479
[8] N.S. Rogado, J. Li, A.W. Sleight, M.A. Subramanian, Magnetocapacitance and magnetoresistance near room temperature in a ferromagnetic semiconductor: La_2NiMnO_6, Adv. Mater. 17 (2005) 2225–2227, https://doi.org/10.1002/adma.200500737
[9] J.Y. Moon, M.K. Kim, Y.J. Choi, N. Lee, Giant anisotropic magnetocaloric effect in double-perovskite Gd_2CoMnO_6 single crystals, Sci. Rep. 7 (2017) 16099, https://doi.org/10.1038/s41598-017-16416-z
[10] J.Y. Moon, M.K. Kim, D.G. Oh, J.H. Kim, H.J. Shin, Y.J. Choi, N. Lee, Anisotropic magnetic properties and giant rotating magnetocaloric effect in double-perovskite Tb_2CoMnO_6, Phys. Rev. B 98 (2018) 174424, https://doi.org/10.1103/PhysRevB.98.174424
[11] L.H. Yin, J. Yang, R.R. Zhang, J.M. Dai, W.H. Song, Y.P. Sun, Multiferroicity and magnetoelectric coupling enhanced large magnetocaloric effect in

$DyFe_{0.5}Cr_{0.5}O_3$, Appl. Phys. Lett. 104 (2014) 2–6, https://doi.org/10.1063/1.4862665
[12] H.-Z. Lin, C.-Y. Hu, P.-H. Lee, A.Z.-Z. Yan, W.-F. Wu, Y.-F. Chen, Y.-K. Wang, Half-metallic property induced by double exchange interaction in the double perovskite $Bi_2BB'O_6$ (B, B′ = 3d transitional metal) via first-principles calculations, Materials 12 (2019) 1844, https://doi.org/10.3390/ma12111844
[13] S.R. Bhandari, D.K. Yadav, B.P. Belbase, M. Zeeshan, B. Sadhukhan, D.P. Rai, R.K. Thapa, G.C. Kaphle, M.P. Ghimire, Electronic, magnetic, optical and thermoelectric properties of $Ca_2Cr_{1-x}Ni_xOsO_6$ double perovskites, RSC Adv. 10 (2020) 16179–16186, https://doi.org/10.1039/C9RA10775D
[14] T. Maiti, M. Saxena, P. Roy, Double perovskite ($Sr_2B'B''O_6$) oxides for high-temperature thermoelectric power generation—a review, J. Mater. Res. 34 (2019) 107–125, https://doi.org/10.1557/jmr.2018.376
[15] H. Wu, X.-L. Shi, W.-D. Liu, M. Li, H. Gao, W. Zhou, Z. Shao, Y. Wang, Q. Liu, Z.-G. Chen, Double perovskite Pr_2CoFeO_6 thermoelectric oxide: Roles of Sr-doping and Micro/nanostructuring, Chem. Eng. J. 425 (2021) 130668, https://doi.org/10.1016/j.cej.2021.130668
[16] R. Pradheesh, H.S. Nair, V. Sankaranarayanan, K. Sethupathi, Exchange bias and memory effect in double perovskite Sr_2FeCoO_6, Appl. Phys. Lett. 101 (2012) 142401, https://doi.org/10.1063/1.4756792
[17] W. Liu, L. Shi, S. Zhou, J. Zhao, Y. Li, Y. Guo, Griffiths phase, spin-phonon coupling, and exchange bias effect in double perovskite Pr_2CoMnO_6, J. Appl. Phys. 116 (2014) 193901, https://doi.org/10.1063/1.4902078
[18] J.K. Murthy, A. Venimadhav, 4 f -3 d exchange coupling induced exchange bias and field induced Hopkinson peak effects in Gd_2CoMnO_6, J. Alloy. Compd. 719 (2017) 341–346, https://doi.org/10.1016/j.jallcom.2017.05.203
[19] J. Navarro, L. Balcells, F. Sandiumenge, M. Bibes, A. Roig, B. Martínez, J. Fontcuberta, Antisite defects and magnetoresistance in Sr_2FeMoO_6 double perovskite, J. Phys. Condens. Matter 13 (2001) 8481–8488, https://doi.org/10.1088/0953-8984/13/37/305
[20] E.E. Ateia, A.T. Mohamed, H. Elshimy, The impact of antisite disorder on the physical properties of $La_2FeB''O_6$ (B″ = Fe, Ni and Co) double perovskites, Appl. Nanosci. 10 (2020) 1489–1499, https://doi.org/10.1007/s13204-020-01356-4
[21] T.-W. Lim, S.-D. Kim, K.-D. Sung, Y.-M. Rhyim, H. Jeen, J. Yun, K.-H. Kim, K.-M. Song, S. Lee, S.-Y. Chung, M. Choi, S.-Y. Choi, Insights into cationic ordering in Re-based double perovskite oxides, Sci. Rep. 6 (2016) 19746, https://doi.org/10.1038/srep19746
[22] L. Wang, S. Liu, X. Chen, B. Li, F. Chi, J. Cheng, Z. Wang, Antisite defect and magnetic frustration in double perovskite Ln_2CuRuO_6 (Ln = La, Pr) compounds, J. Supercond. Nov. Magn. 34 (2021) 851–857, https://doi.org/10.1007/s10948-020-05763-0
[23] M.K. Kim, J.Y. Moon, H.Y. Choi, S.H. Oh, N. Lee, Y.J. Choi, Investigation of the magnetic properties in double perovskite R_2CoMnO_6 single crystals (R = rare earth: La to Lu), J. Phys. Condens. Matter 27 (2015) 426002, https://doi.org/10.1088/0953-8984/27/42/426002
[24] V.A. Khomchenko, I.O. Troyanchuk, A.P. Sazonov, V.V. Sikolenko, H. Szymczak, R. Szymczak, Metamagnetic behaviour in $TbCo_{0.5}Mn_{0.5}O_{3.06}$ perovskite, J. Phys. Condens. Matter 18 (2006) 9541–9548, https://doi.org/10.1088/0953-8984/18/42/001
[25] A.N. Vasiliev, O.S. Volkova, L.S. Lobanovskii, I.O. Troyanchuk, Z. Hu, L.H. Tjeng, D.I. Khomskii, H.-J. Lin, C.T. Chen, N. Tristan, F. Kretzschmar, R. Klingeler, B. Büchner, Valence states and metamagnetic phase transition in partially B-site-disordered perovskite $EuMn_{0.5}Co_{0.5}O_3$, Phys. Rev. B. 77 (2008) 104442, https://doi.org/10.1103/PhysRevB.77.104442
[26] R.P. Madhogaria, R. Das, E.M. Clements, V. Kalappattil, M.H. Phan, H. Srikanth, N.T. Dang, D.P. Kozlenko, N.S. Bingham, Evidence of long-range ferromagnetic order and spin frustration effects in the double perovskite La_2CoMnO_6, Phys. Rev. B. 99 (2019) 104436, https://doi.org/10.1103/PhysRevB.99.104436
[27] P.R. Mandal, R.C. Sahoo, T.K. Nath, A comparative study of structural, magnetic, dielectric behaviors and impedance spectroscopy for bulk and nanometric double perovskite Sm_2CoMnO_6, Mater. Res. Express 1 (2014) 046108, https://doi.org/10.1088/2053-1591/1/4/046108
[28] A. Haque, R. Das, D. Ghosh, M. Vasundhara, A. Gayen, A.K. Kundu, M.M. Seikh, Observation of Predominant Long-Range Ordering by Overcoming the Magnetic Frustration in Cu-Doped La_2MnCoO_6, J. Phys. Chem. C 125 (2021) 3088–3101, https://doi.org/10.1021/acs.jpcc.0c09120
[29] S.A. Ivanov, T. Sarkar, G.V. Bazuev, M.V. Kuznetsov, P. Nordblad, R. Mathieu, Modification of the structure and magnetic properties of ceramic La_2CoMnO_6 with Ru doping, J. Alloy. Compd. 752 (2018) 420–430, https://doi.org/10.1016/j.jallcom.2018.04.164
[30] L. Wang, W. Zhou, D. Wang, Q. Cao, Q. Xu, Y. Du, Effect of metamagnetism on multiferroic property in double perovskite Sm_2CoMnO_6, J. Appl. Phys. 117 (2015) 17D914, https://doi.org/10.1063/1.4917517
[31] C.L. Li, L.G. Wang, X.X. Li, C.M. Zhu, R. Zhang, H.W. Wang, S.L. Yuan, Magnetic field-induced metamagnetism and magnetocaloric effect in double perovskites Re_2CoMnO_6 (Re = Sm, Dy), Mater. Chem. Phys. 202 (2017) 76–81, https://doi.org/10.1016/j.matchemphys.2017.09.009
[32] S.K. Giri, R.C. Sahoo, P. Dasgupta, A. Poddar, T.K. Nath, Giant spontaneous exchange bias effect in $Sm_{1.5}Ca_{0.5}CoMnO_6$ perovskite, J. Phys. D. Appl. Phys. 49 (2016) 165002, https://doi.org/10.1088/0022-3727/49/16/165002
[33] R.C. Sahoo, D. Paladhi, P. Dasgupta, A. Poddar, R. Singh, A. Das, T.K. Nath, Antisite-disorder driven large exchange bias effect in phase separated $La_{1.5}Ca_{0.5}CoMnO_6$ double perovskite, J. Magn. Magn. Mater. 428 (2017) 86–91, https://doi.org/10.1016/j.jmmm.2016.12.018
[34] J. Krishna Murthy, K.D. Chandrasekhar, H.C. Wu, H.D. Yang, J.Y. Lin, A. Venimadhav, Antisite disorder driven spontaneous exchange bias effect in $La_{2-x}Sr_xCoMnO_6$ ($0 \leqslant x \leqslant 1$), J. Phys. Condens. Matter 28 (2016) 086003, https://doi.org/10.1088/0953-8984/28/8/086003
[35] L. Lutterotti, S. Matthies, H.-R. Wenk, MAUD: a friendly Java program for material analysis using diffraction IUCr Newsl. Cpd., 1999, pp. 14–15.(https://www.iucr.org/__data/assets/pdf_file/0016/21634/cpd21.pdf).
[36] X. Luo, L. Bai, J. Xing, X. Zhu, D. Xu, B. Xie, Z. Gan, G. Li, H. Liang, Ordered Mesoporous Cobalt Containing Perovskite as a High-Performance Heterogeneous Catalyst in Activation of Peroxymonosulfate, ACS Appl. Mater. Interfaces 11 (2019) 35720–35728, https://doi.org/10.1021/acsami.9b11322
[37] F. Liu, J. Li, Q. Li, Y. Wang, X. Zhao, Y. Hua, C. Wang, X. Liu, High pressure synthesis structure, and multiferroic properties of two perovskite compounds Y_2FeMnO_6 and Y_2CrMnO_6, Dalton Trans. 43 (2014) 1691–1698, https://doi.org/10.1039/C3DT52336E
[38] A. Vansteenkiste, J. Leliaert, M. Dvornik, M. Helsen, F. Garcia-Sanchez, B.Van Waeyenberge, The design and verification of MuMax3, AIP Adv. 4 (2014) 107133, https://doi.org/10.1063/1.4899186
[39] R.C. Sahoo, S. Das, S.K. Giri, D. Paladhi, T.K. Nath, Size modulated Griffiths phase and spin dynamics in double perovskite $Sm_{1.5}Ca_{0.5}CoMnO_6$, J. Magn. Magn. Mater. 469 (2019) 161–170, https://doi.org/10.1016/j.jmmm.2018.08.060
[40] Y. Cao, W. Li, K. Xu, Y. Zhang, T. Ji, R. Zou, J. Yang, Z. Qin, J. Hu, $MnMoO_4{\cdot}4H_2O$ nanoplates grown on a Ni foam substrate for excellent electrochemical properties, J. Mater. Chem. A 2 (2014) 20723–20728, https://doi.org/10.1039/C4TA04019H
[41] Y. Xu, J. Sherwood, Y. Qin, R.A. Holler, Y. Bao, A general approach to the synthesis and detailed characterization of magnetic ferrite nanocubes, Nanoscale 7 (2015) 12641–12649, https://doi.org/10.1039/C5NR03096J
[42] M. Oku, K. Hirokawa, X-ray photoelectron spectroscopy of manganese-oxygen systems, J. Electron Spectrosc. Relat. Phenom. 7 (1975) 465–473, https://doi.org/10.1016/0368-2048(75)85010-9
[43] Y. Li, D. Li, S. Fan, T. Yang, Q. Zhou, Facile template synthesis of dumbbell-like Mn_2O_3 with oxygen vacancies for efficient degradation of organic pollutants by activating peroxymonosulfate, Catal. Sci. Technol. 10 (2020) 864–875, https://doi.org/10.1039/C9CY01849B
[44] Y. Fu, Q. Wei, G. Zhang, X. Wang, J. Zhang, Y. Hu, D. Wang, L. Zuin, T. Zhou, Y. Wu, S. Sun, High-performance reversible aqueous Zn-ion battery based on porous MnO_x nanorods coated by MOF-derived N-doped carbon, Adv. Energy Mater. 8 (2018) 1801445, https://doi.org/10.1002/aenm.201801445
[45] H. Xia, D. Zhu, Z. Luo, Y. Yu, X. Shi, G. Yuan, J. Xie, Hierarchically structured Co_3O_4@Pt@MnO_2 nanowire arrays for high-performance supercapacitors, Sci. Rep. 3 (2013) 2978, https://doi.org/10.1038/srep02978
[46] X. Wang, W. Li, X. Wang, J. Zhang, L. Sun, C. Gao, J. Shang, Y. Hu, Q. Zhu, Electrochemical properties of $NiCoO_2$ synthesized by hydrothermal method, RSC Adv. 7 (2017) 50753–50759, https://doi.org/10.1039/C7RA10232A
[47] J. Si, S. Xiao, Y. Wang, L. Zhu, X. Xia, Z. Huang, Y. Gao, Sub-nanometer Co_3O_4 clusters anchored on TiO_2 (B) nano-sheets: Pt replaceable Co-catalysts for H_2 evolution, Nanoscale 10 (2018) 2596–2602, https://doi.org/10.1039/C7NR07336D
[48] Q. Liu, H. Yang, H. Dong, W. Zhang, B. Bian, Q. He, J. Yang, X. Meng, Z. Tian, G. Zhao, Effects of preparation method and Sm_2O_3 promoter on CO methanation by a mesoporous $NiO–Sm_2O_3/Al_2O_3$ catalyst, N. J. Chem. 42 (2018) 13096–13106, https://doi.org/10.1039/C8NJ02282H
[49] I.N. Bhatti, I.N. Bhatti, R.N. Mahato, M.A.H. Ahsan, Magnetic behavior, Griffiths phase and magneto-transport study in 3d based nano-crystalline double perovskite Pr_2CoMnO_6, Phys. Lett. A 383 (2019) 2326–2332, https://doi.org/10.1016/j.physleta.2019.04.036
[50] S. Araujo-Barbosa, O.J.B.J. Marques, E.L.T. França, F.L.A. Machado, J.C. Mantilla, Magnetic properties of the double perovskites $Sm_2Mn_{1+x}Co_{1-x}O_6$ (x = 0, 0.05, 0.12 and 0.26), J. Phys. Condens. Matter 32 (2020) 105803, https://doi.org/10.1088/1361-648X/ab5988
[51] R. Kamel, A. Tozri, E. Dhahri, E.K. Hlil, Anomalous behavior above the Curie temperature in $(Nd_{1-x}Gd_x)_{0.55}Sr_{0.45}MnO_3$ (x = 0, 0.1, 0.3 and 0.5), RSC Adv. 9 (2019) 27541–27548, https://doi.org/10.1039/C9RA03303C
[52] S. Ghosh, A. Kumar, A. Pal, P. Singh, P. Gupta, K. Anand, U.K. Gautam, A.K. Ghosh, S. Chatterjee, Existence of exchange bias and Griffith phase in $(Tb_{1-x}Ce_x)MnO_3$, J. Magn. Magn. Mater. 500 (2020) 166261, https://doi.org/10.1016/j.jmmm.2019.166261
[53] H.S. Nair, T. Chatterji, A.M. Strydom, Antisite disorder-induced exchange bias effect in multiferroic Y_2CoMnO_6, Appl. Phys. Lett. 106 (2015) 022407, https://doi.org/10.1063/1.4906204
[54] T. Asaka, X.Z. Yu, Y. Tomioka, Y. Kaneko, T. Nagai, K. Kimoto, K. Ishizuka, Y. Tokura, Y. Matsui, Strong pinning effect and magnetic nanodomain formation by coupling between magnetic and crystallographic domains in the ordered double perovskite Ba_2FeMoO_6, Phys. Rev. B. 75 (2007) 184440, https://doi.org/10.1103/PhysRevB.75.184440
[55] J. Leliaert, B. Van de Wiele, A. Vansteenkiste, L. Laurson, G. Durin, L. Dupré, B.Van Waeyenberge, Current-driven domain wall mobility in polycrystalline permalloy nanowires: a numerical study, J. Appl. Phys. 115 (2014) 233903, https://doi.org/10.1063/1.4883297
[56] M. Yi, O. Gutfleisch, B.-X. Xu, Micromagnetic simulations on the grain shape effect in Nd-Fe-B magnets, J. Appl. Phys. 120 (2016) 033903, https://doi.org/10.1063/1.4958697
[57] M.-R. Li, J.P. Hodges, M. Retuerto, Z. Deng, P.W. Stephens, M.C. Croft, X. Deng, G. Kotliar, J. Sánchez-Benítez, D. Walker, M. Greenblatt, Mn_2MnReO_6: synthesis and magnetic structure determination of a new transition-metal-only double perovskite canted antiferromagnet, Chem. Mater. 28 (2016) 3148–3158, https://doi.org/10.1021/acs.chemmater.6b00755

[58] J. Krishna Murthy, A. Venimadhav, Giant zero field cooled spontaneous exchange bias effect in phase separated $La_{1.5}Sr_{0.5}CoMnO_6$, Appl. Phys. Lett. 103 (2013) 252410, https://doi.org/10.1063/1.4855135
[59] M.-R. Li, P.W. Stephens, M. Croft, Z. Deng, W. Li, C. Jin, M. Retuerto, J.P. Hodges, C.E. Frank, M. Wu, D. Walker, M. Greenblatt, $Mn_2(Fe_{0.8}Mo_{0.2})MoO_6$: a double perovskite with multiple transition metal sublattice magnetic effects, Chem. Mater. 30 (2018) 4508–4514, https://doi.org/10.1021/acs.chemmater.8b00250
[60] M.S. Lee, T.A. Wynn, E. Folven, R.V. Chopdekar, A. Scholl, S.T. Retterer, J.K. Grepstad, Y. Takamura, Temperature dependence of ferromagnet-antiferromagnet spin alignment and coercivity in epitaxial micromagnet bilayers, Phys. Rev. Mater. 1 (2017) 014402, https://doi.org/10.1103/PhysRevMaterials.1.014402
[61] D. Djuhana, L. Rohman, D.H. Kim, Micromagnetic calculation of the dynamic susceptibility spectra in LSMO ($La_{0.7}Sr_{0.3}MnO_3$) ferromagnetic nanopillars, J. Magn. 22 (2017) 364–368, https://doi.org/10.4283/JMAG.2017.22.3.364
[62] J. Leliaert, J. Mulkers, J. De Clercq, A. Coene, M. Dvornik, B. Van Waeyenberge, Adaptively time stepping the stochastic Landau-Lifshitz-Gilbert equation at nonzero temperature: Implementation and validation in MuMax 3, AIP Adv. 7 (2017) 125010, https://doi.org/10.1063/1.5003957
[63] M.B. Hahn, Temperature in micromagnetism: cell size and scaling effects of the stochastic Landau–Lifshitz equation, J. Phys. Commun. 3 (2019) 075009, https://doi.org/10.1088/2399-6528/ab31e6
[64] J. De Clercq, A. Vansteenkiste, M. Abes, K. Temst, B.Van Waeyenberge, Modelling exchange bias with MuMax3, J. Phys. D. Appl. Phys. 49 (2016) 435001, https://doi.org/10.1088/0022-3727/49/43/435001
[65] L.T. Coutrim, D. Rigitano, C. Macchiutti, T.J.A. Mori, R. Lora-Serrano, E. Granado, E. Sadrollahi, F.J. Litterst, M.B. Fontes, E. Baggio-Saitovitch, E.M. Bittar, L. Bufaiçal, Zero-field-cooled exchange bias effect in phase-segregated La2−xAxCoMnO6−δ (A = Ba,Ca,Sr; x = 0, 0.5), Phys. Rev. B 100 (2019) 054428, https://doi.org/10.1103/PhysRevB.100.054428
[66] L.T. Coutrim, E.M. Bittar, F. Garcia, L. Bufaiçal, Influence of spin glass-like magnetic relaxation on the zero-field-cooled exchange bias effect, Phys. Rev. B. 98 (2018) 064426, https://doi.org/10.1103/PhysRevB.98.064426